Using *MAT_213 and *MAT_187 to Predict Failure in Unidirectional Composites

Bilal Khaled, Loukham Shyamsunder, Josh Robbins,
Yatin Parakhiya, and Subramaniam D. Rajan
School of Sustainable Engineering and the Built Environment,
Arizona State University, Tempe, AZ

Abstract

*Failure in composite materials is due to various complex mechanisms often occurring simultaneously. The heterogeneous, anisotropic nature of composites provides challenges in deriving analytical models for failure similar to what has historically been done with homogeneous, isotropic metals. However, as composites continue to be used in the design of large structures, finite element material models which homogenize the composite response become the only logical choice as modeling the entire microstructure is currently impractical. Thus, relating the microscale behavior caused by the macroscopic excitations is required. A modeling methodology where plasticity, damage, and failure related experimental data are obtained for each constituent and subsequently used to generate high fidelity computational micromechanical models. The ultimate goal is to utilize information from the micromechanical computational models to drive the failure sub-model of *MAT_213 in LS-DYNA®. The first step is to obtain high fidelity experimental data and refine the respective material models for each constituent. This research presents the experimental results from tests performed on the F3900 epoxy resin. The data is then used to populate the input deck for *MAT_187 in LS-DYNA. Verifications tests are presented showing how the derived experimental data performed in virtual finite element tests.*

Introduction

Predicting failure in composites poses a significant challenge. There have been concerted efforts to identify the most accurate theories of failure [Hinton and Kaddour, 2012; Kaddour et al., 2013] yet there is still no consensus on the most effective techniques. A method that has recently gained popularity is to use micromechanical or mesomechanical computational modeling schemes to explicitly model the individual constituents of the composite and perform *virtual tests* using finite element methods. This method provides advantages over experimental techniques since generating arbitrary triaxial states of stress poses many challenges [Olsson, 2012]. The overall goal of this research is to generate a tabulated failure surface for the T800S/F3900 carbon fiber/epoxy resin unidirectional composite through virtual tests to use as input for the failure modeling capabilities of *MAT_213 [Goldberg et al., 2018;Hoffarth, 2016; ; Khaled et al., 2018; Khaled et al., 2019; Shyamsunder et al., 2020]. The failure surface will then be used in predicting failure under a variety of loading scenarios, e.g. crush, projectile impact events, etc. This paper focuses on the first step of the process: deriving reliable experimental data for the individual composite constituents, namely the epoxy resin. The paper focuses on the experimentation performed on the F3900 resin necessary to populate the *MAT_187 input deck [Kolling et al., 2005; Du Bois et al., 2006]. Verification and numerical calibration to further refine the *MAT_187 input deck is also presented.

*MAT_187 Background

LS-DYNA's *MAT_187 was used to model the epoxy matrix. MAT187 is a semi-analytical model for polymers which includes provisions for rate-dependent plasticity, uncoupled damage, and equivalent plastic strain dependent failure. The rate-dependent plasticity formulation is governed by a non-associative formulation where the base form yield function takes the following form

$$f = \sigma_{vm} - A_0 - A_1 p - A_2 p^2 \leq 0 \tag{1}$$

where σ_{vm} is the von Mises stress, p is the pressure, $-\frac{tr(\boldsymbol{\sigma})}{3}$, and A_i are the coefficients that define the shape of yield surface. The three coefficients in Eq. (1) are determined directly from uniaxial tension, compression, and shear experiments. The evolution of yield surface is dictated by the experimental data as the entire tabulated stress-plastic strain curve for each of the three experiments is provided as input. In addition to the data from uniaxial tests, equibiaxial tension and compression test data may also be provided. Doing so results in an alternate from of the yield criterion in the form of a piecewise linear relationship shown schematically in Figure 1.

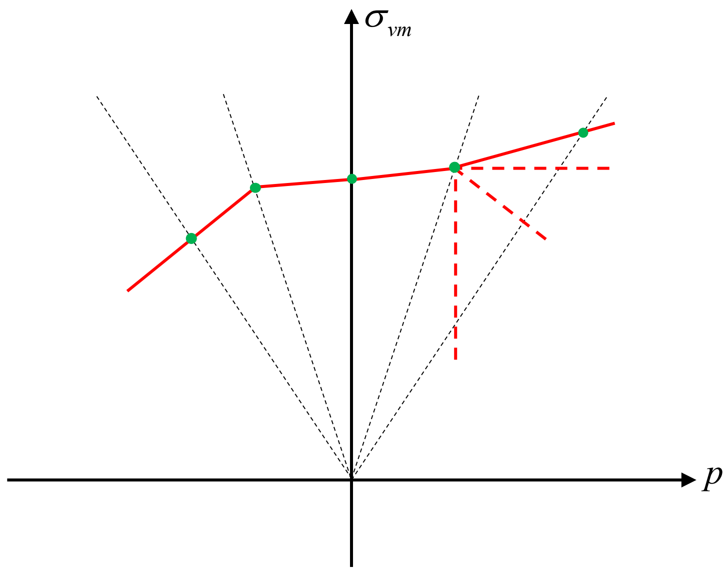

Figure 1. Piecewise linear yield surface relating von Mises stress and pressure

The red line denotes the piecewise linear yield surface in stress invariant space while the green points represent the points provided by the user as input through either stress-plastic curves or through single parameters. The point where the yield surface intersects the equibiaxial compression loading path is dictated by the parameter RBCFAC [LSTC, 2019]. RBCFAC is the ratio between yield in biaxial compression and uniaxial compression. The dashed red lines represent possible values of RBCFAC and how they influence the shape of the yield surface. Uniaxial tension stress-plastic strain data at multiple strain rates may be included if available and necessary resulting in rate-dependent yield surface evolution. Rate dependence of uniaxial shear and compression is assumed to follow the same trend as the uniaxial tension data. The non-associative flow rule is given as

$$\dot{\boldsymbol{\varepsilon}}_p = \dot{\lambda} \frac{\partial g}{\partial \boldsymbol{\sigma}} \tag{2}$$

where $\dot{\lambda}$ is the plastic multiplier and g is the plastic potential function given by

$$g = \sqrt{\sigma_{vm}^2 - \alpha p^2} \tag{3}$$

where the coefficient α is related to the plastic Poisson's ratio, ν_p that is a user defined quantity either provided as a constant or as a function of plastic strain from uniaxial compression and tension tests which provides the ability to handle asymmetric plastic flow.

The damage modeling capabilities of MAT187 were not used in the current research work and thus details will not be provided. *MAT_187 also provides provisions to handle material failure and element erosion. Two of the salient parameters used in this research are the *equivalent plastic strain at failure*, $\bar{\varepsilon}_p^f$, and the *equivalent plastic strain at rupture*, $\bar{\varepsilon}_p^r$. The former defines the onset of failure where stresses begin degrading to a value of zero while the latter defines the point where the stresses in a *failed* element become zero resulting in the element being eroded from the model. The stress degradation process is shown schematically in Figure 2.

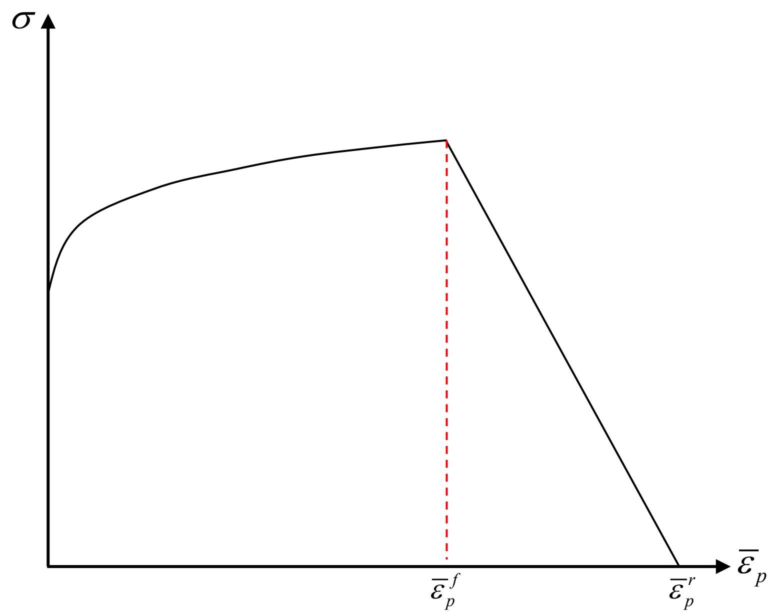

Figure 2. Stress degradation process showing equivalent plastic strain at failure and equivalent plastic strain at rupture

The equivalent plastic strain rate takes the commonly known form

$$\dot{\varepsilon}_p = \sqrt{\frac{2}{3}\dot{\boldsymbol{\varepsilon}}_{dp} : \dot{\boldsymbol{\varepsilon}}_{dp}} \tag{4}$$

where $\dot{\varepsilon}_p$ is the equivalent plastic strain rate and $\dot{\boldsymbol{\varepsilon}}_{dp}$ is the deviatoric component of the plastic strain rate tensor which is directly dependent on the plastic multiplier, $\dot{\lambda}$ [Kolling et al., 2005]. The value of $\bar{\varepsilon}_p^f$ may be defined as both a function of plastic strain rate and triaxiality, $T = \frac{p}{\sigma_{vm}}$. The dependence of failure on triaxiality allows the user to define failure for various mode of loading. In the case of this research, data was acquired for uniaxial tension $\left(T = -\frac{1}{3}\right)$, uniaxial shear $(T = 0)$, and uniaxial compression $\left(T = \frac{1}{3}\right)$. The experimental methods, results, and post-processing techniques used to derive each of the *MAT_187 parameters described for the F3900 epoxy matrix are provided in the next section.

Experimental Methods and Results

Uniaxial tension, compression, and shear experiments were performed on the neat F3900 epoxy resin at quasi-static strain rates and room temperature conditions (QS-RT). Digital image correlation (DIC) was used to measure strain fields on the surface of each test specimen, while a 20-kip load cell, MTS model #661.21A-03, was used to measure force transferred to the specimens. Each of the specimens were manufactured from neat resin panels of 0.160” nominal thickness using a waterjet.

Uniaxial Tension

The specimen dimensions and geometry, shown in Figure 3, are taken from ASTM D638-14 [D20 Committee, 2014] for a Type II specimen to promote failure in the gage section.

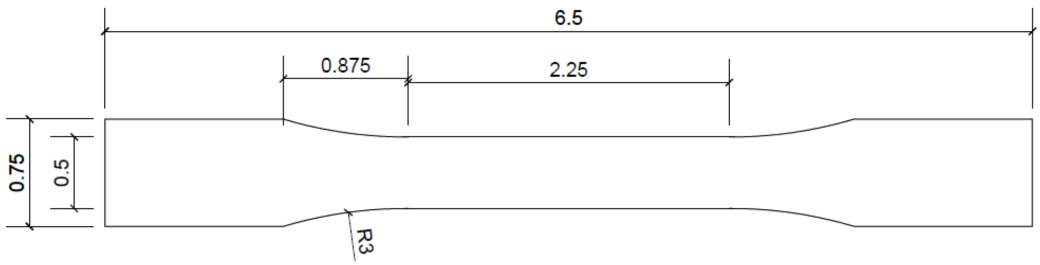

Figure 3. Typical specimen geometry and layout for uniaxial tension specimens (dimensions in inches)

A typical specimen after testing is shown in Figure 4.

Figure 4. Typical failed uniaxial tension specimen

The experimental results are converted from engineering stress and strain quantities to true stress and strain quantities as this is the form expected by *MAT_187. The expressions used for the conversion are shown below.

$$\sigma^{true} = \sigma^{eng}\left(1+\varepsilon^{eng}\right) \tag{5}$$

$$\varepsilon^{true} = \ln\left(1+\varepsilon^{eng}\right) \tag{6}$$

From here, the results of multiple experimental replicates are averaged, and a single representative curve is generated. This process is described in more detail in Khaled et al. [Khaled et al., 2018]. The representative curve is then converted from true stress-true total strain to true stress-true plastic strain using the following equation.

$$\varepsilon_{pt} = \varepsilon_t - \frac{\sigma_t}{E} \tag{7}$$

This process is used for all experiments presented in this document. The final form of the curve used as input to *MAT_187 is shown in Figure 5.

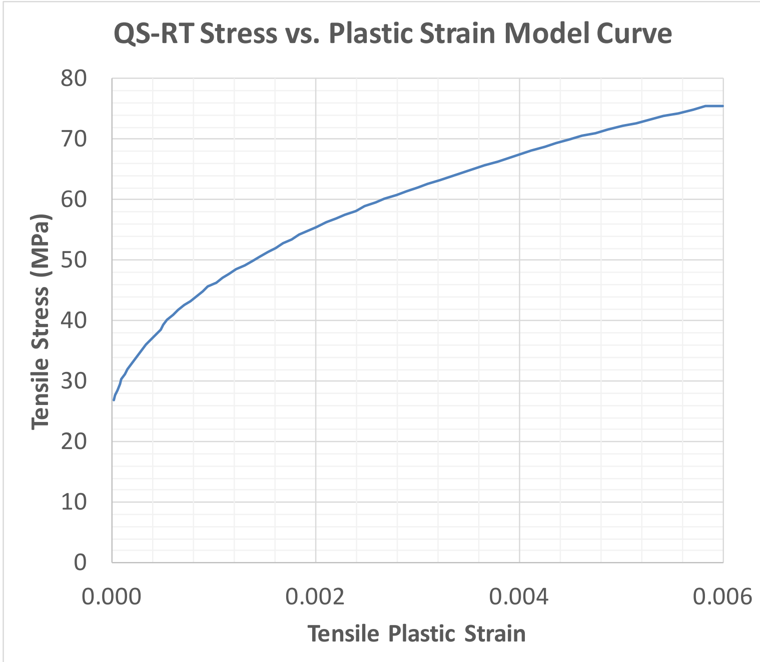

Figure 5. Uniaxial tension true stress-true plastic strain input curve

Uniaxial Compression

Recommendations for specimen geometry and dimensions were taken from ASTM D6641-16 [D30 Committee, 2016]. However, to aid in the testing of several specimens, the dimensions were scaled for use with a modified combined loading compression (CLC) fixture manufacture by Wyoming Test Fixtures[1]. The specimen dimensions and geometry along with the test setup are shown in Figure 6.

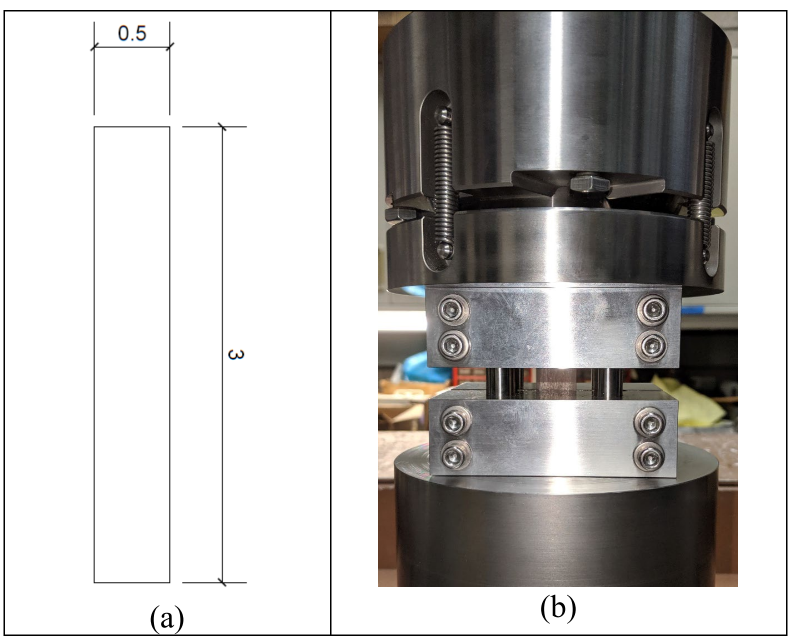

Figure 6. (a) Typical specimen geometry and layout (dimensions in inches) for uniaxial compression specimens and (b) CLC test fixture in between compression platens.

[1] http://wyomingtestfixtures.com/products/compression/wyoming-combined-loading-compression-test-fixture-astm-d-6641/

A typical specimen after testing is shown in Figure 7.

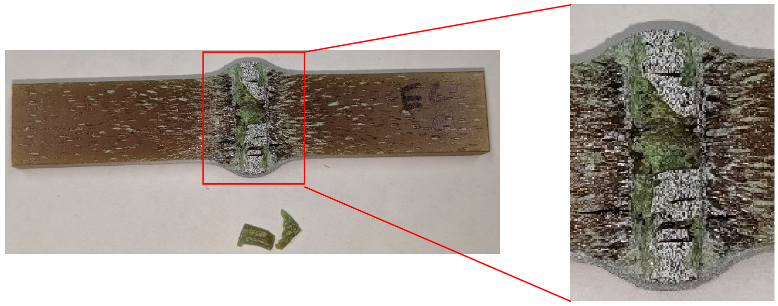

Figure 7. Typical failed uniaxial compression specimen

The compression specimen underwent significant lateral deformation as shown in Figure 7. This was likely due to the friction caused by the gripping fixture at the top and bottom of the gage section. Additionally, crazing is seen on the surface as evidenced by the discoloration of the material after testing. Figure 8 shows how the longitudinal strain field evolved during the tests.

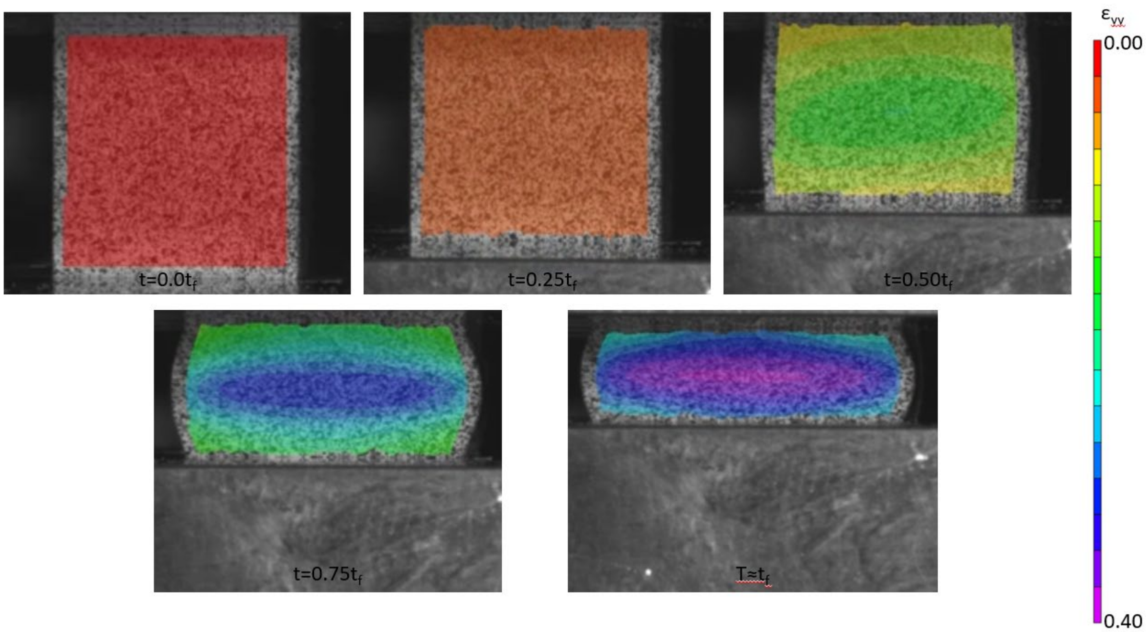

Figure 8. Evolution of longitudinal strain field from typical uniaxial compression test

Figure 8 shows that, initially, the strain field is fairly constant on the surface of the specimen. However, as the deformation increases, the strain becomes larger in the center of the specimen than at the boundaries. This roughly coincides with the point on the stress-plastic strain curve where the material exhibits “re-stiffening” behavior, shown in Figure 9. Analysis of the strain field shows that the specimen is likely no longer in pure compression at this point. Rather, the region near the boundary is experiencing a multiaxial state of stress. Figure 9 shows the uniaxial compression curve used as input to *MAT_187.

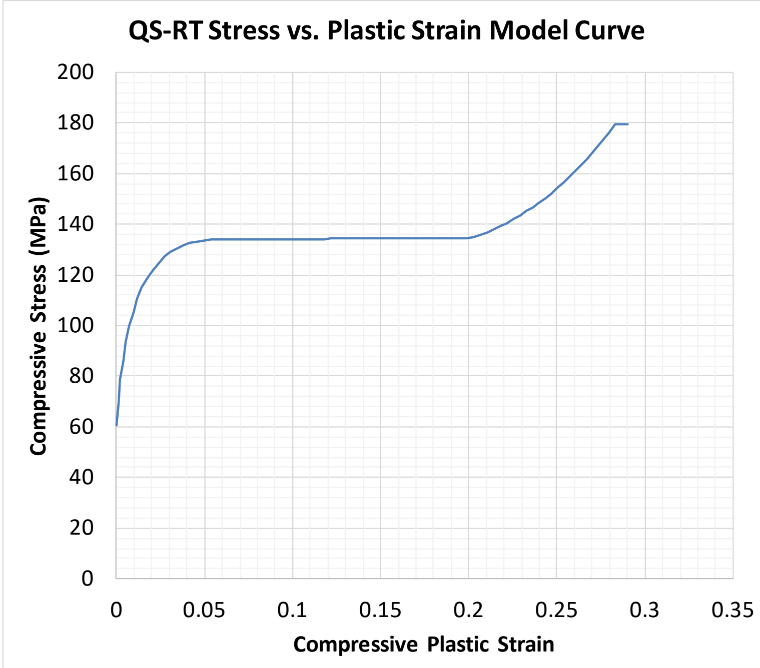

Figure 9. Uniaxial compression true stress-true plastic strain input curve

Uniaxial Shear

Recommendations for specimen geometry and dimensions were taken from ASTM D5379 [D30 Committee, 2019]. Tests were performed using an Iosipescu shear test fixture manufactured by Wyoming Test Fixtures[2]. The specimen dimensions and geometry along with the testing setup are shown in Figure 10.

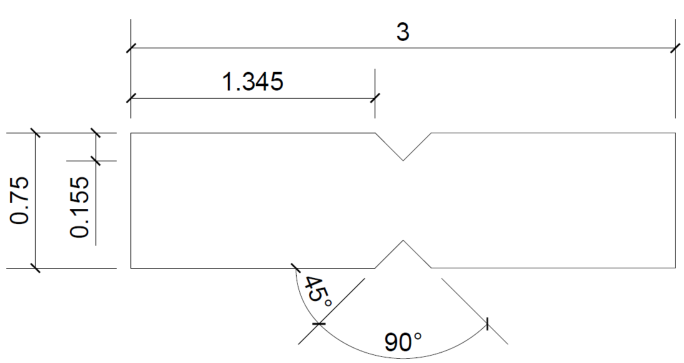

(a)

(b)

Figure 10. (a) Typical specimen geometry and layout (dimensions in inches) for Iosipescu shear specimens and (b) Iosipescu shear test fixture

[2] http://wyomingtestfixtures.com/products/shear/iosipescu-shear-test-fixture-astm-d-5379/

A typical specimen after testing is shown in Figure 11.

Figure 11. Typical failed Iosipescu shear specimen

The failure pattern exhibited by the specimen in Figure 11 indicates a presence of significant transverse and longitudinal strains meaning the specimen is likely not in a state of pure shear. This is reinforced by the DIC images shown in Figure 12 where the in-plane strain field is antisymmetric.

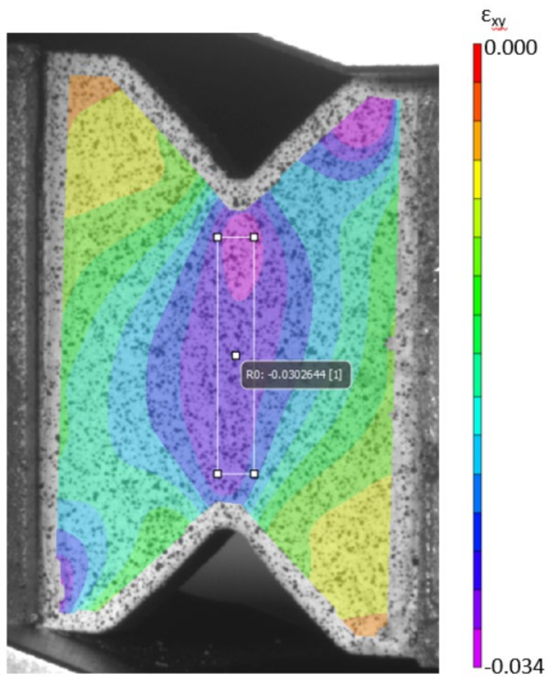

Figure 12. In-plane shear strain field near end of Iosipescu shear test

The skewed nature of the strain field in the Iosipescu shear test has been confirmed in previously conducted tests [Liu and Piggott, 1995]. This likely due to the presence of bending in the specimen. The technique to derive shear properties of the matrix must be refined. However, the data from this experiment was used moving forward in this research. Figure 13 shows the uniaxial shear curve used as input to *MAT_187.

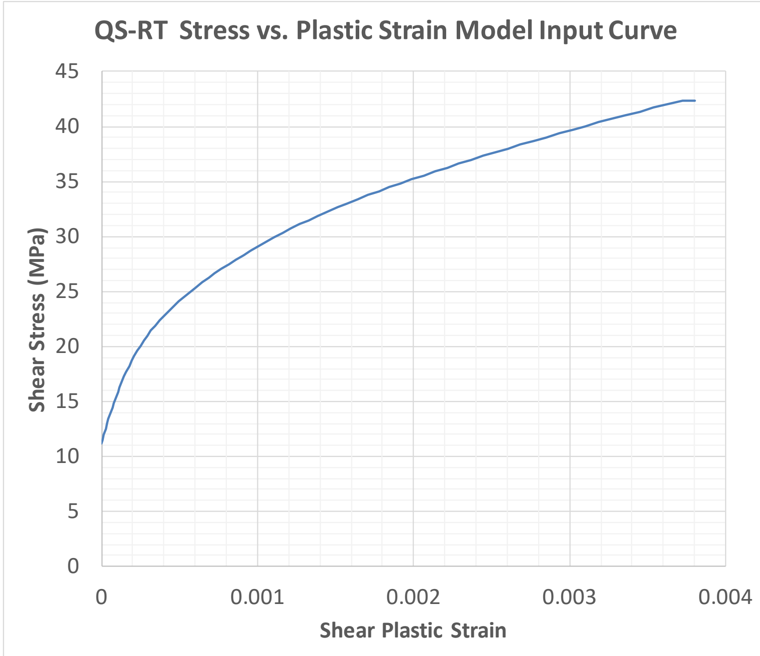

Figure 13. Uniaxial compression true stress-true plastic strain input curve

Verification Tests

Single element (SE) and multi-element (ME) verification tests were performed using LS-DYNA and *MAT_187 to refine the F3900 resin modeling strategy. The focus was on fine tuning the plasticity and failure parameters that are challenging to obtain directly from experimental data, namely, the equivalent plastic strain at failure $\left(\bar{\varepsilon}_p^f\right)$ and the equivalent plastic strain at rupture $\left(\bar{\varepsilon}_p^r\right)$. The parameters were varied until the best fit between experimental data and the simulations was found.

<u>Single Element (SE) Verification Tests</u>

SE were utilized to ensure all data used to drive the models were properly formatted and consistent. Unit volume cubes were generated with appropriate boundary conditions to generate stress states corresponding to uniaxial tension, uniaxial compression, and uniaxial shear. Each of the simulations was performed under displacement control. Figure 14 shows schematics for each finite element model.

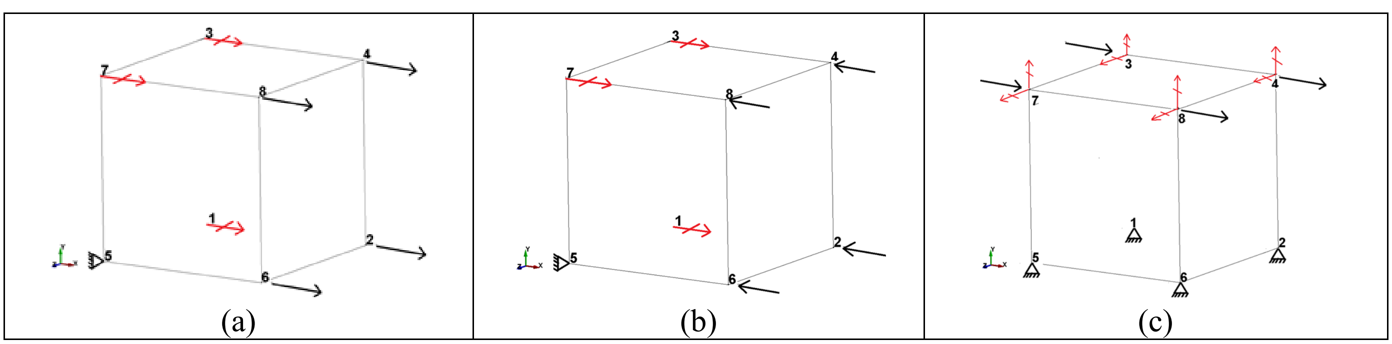

Figure 14. Single element models for (a) uniaxial tension, (b) uniaxial compression, and (c) uniaxial shear (red arrows indicate restrained degrees of freedom, pins indicate all degrees of freedom are restrained)

In addition to stress-plastic strain curves shown in Figure 5, Figure 9, and Figure 13 respectively, the plastic Poisson's ratio (ν_p) was computed from the uniaxial tension. The details of the data reduction technique can be found in a previous publication [Khaled, 2019].The initial value of the equivalent plastic strain at failure $(\bar{\varepsilon}_p^f)$ was set to the plastic strain at failure under uniaxial tension from the experimental data, 0.006. Additionally, *MAT_187 has a feature wherein the value of $\bar{\varepsilon}_p^f$ may be input as a tabulated curve using triaxiality as the independent variable through scale factors. The value of $\bar{\varepsilon}_p^r$ was initially set to a value of 0 since stress degradation was not a concern in the SE verification tests. Table 1 shows a summary of the failure parameters used in the SE verification tests.

Table 1. Equivalent Plastic Strain Failure Scale Factors as a Function of Stress Triaxiality

Stress Condition	**Resulting Triaxiality**	**Scale Factor**
Uniaxial Tension	-0.333	1.00
Uniaxial Shear	0.000	0.78
Uniaxial Compression	0.333	48.565

The results of the single element verification simulations are shown in Figure 15.

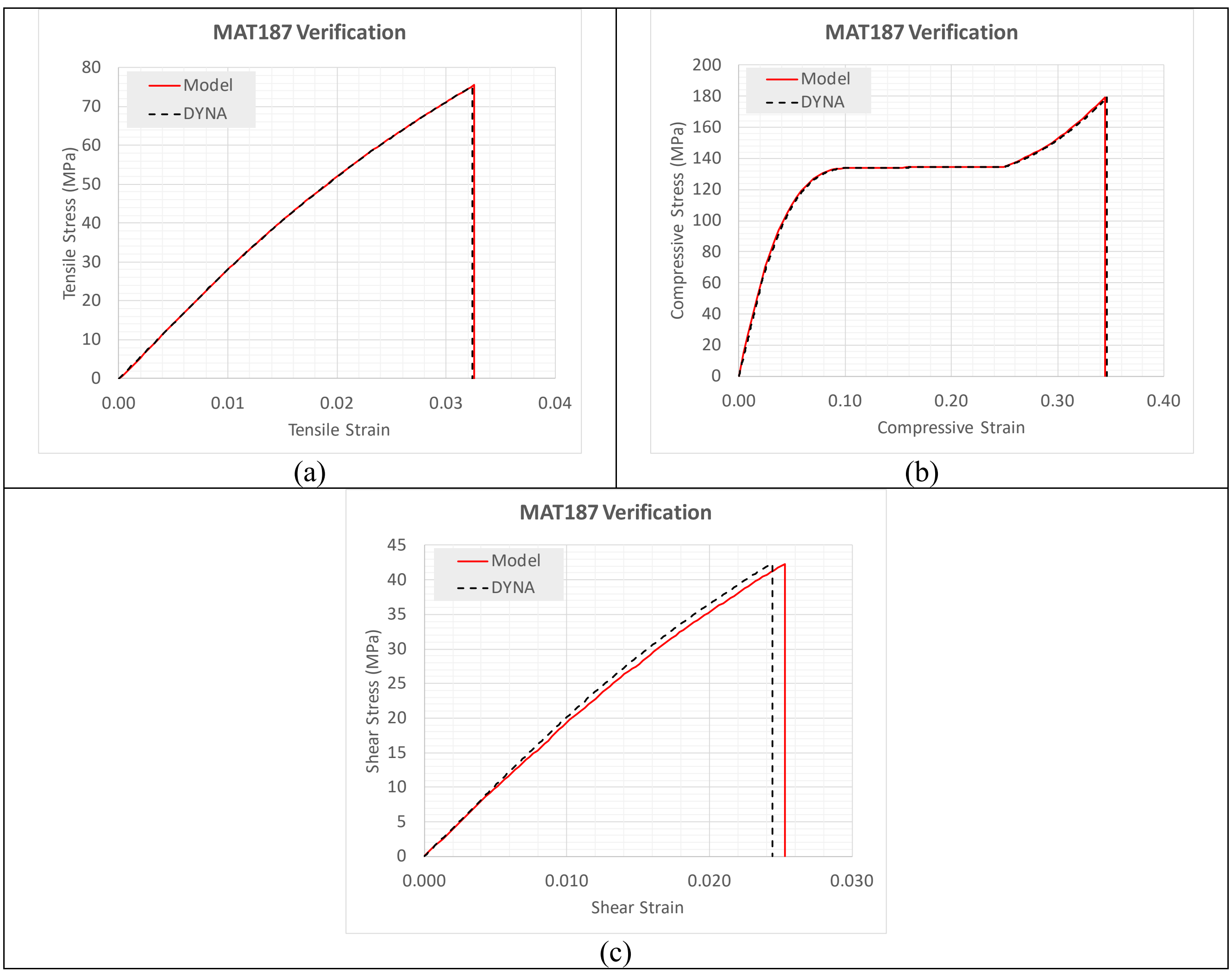

Figure 15. Results of SE verification tests exercising both plasticity parameters and failure parameters (a) uniaxial tension, (b) uniaxial compression, and (c) uniaxial shear

The results of the SE verification test show a fair match with experimental data. This study was used as a first order investigation to identify any major issues with the modeling strategy. A multi-element verification test was also performed to further refine the model.

Multi-element (ME) Verification Tests

The multi-element verification tests sought to model the uniaxial compression experimental conditions. The simulations were used to calibrate the values of both RBCFAC and $\overline{\varepsilon}_p^r$ since the experimental DIC images showed that the state of stress may not be uniaxial. Both quantities of interest were adjusted until a best fit with experimental data was achieved. A quarter symmetric model was used to save on computational cost. Figure 16 shows the details of the finite element model used for the simulations.

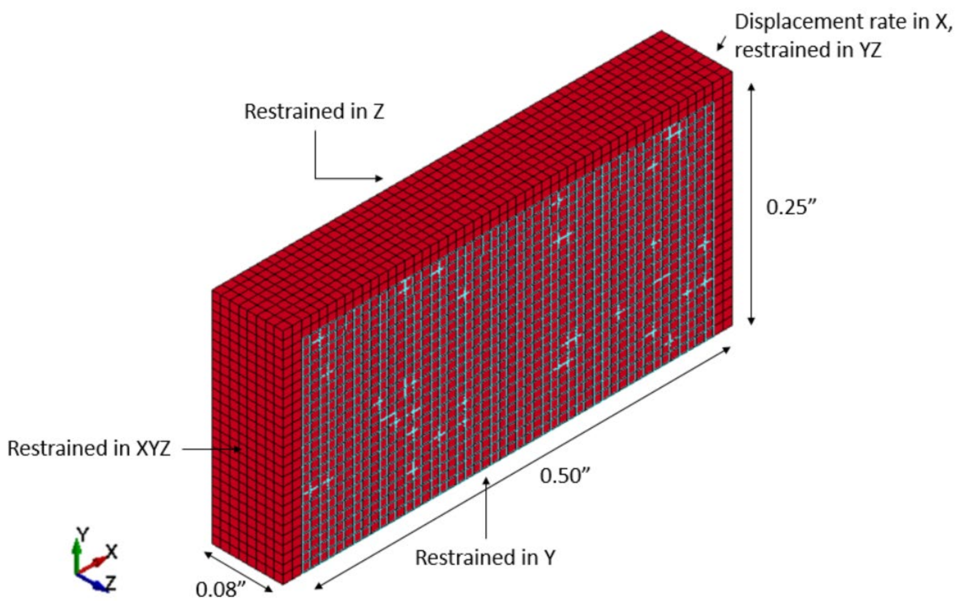

Figure 16. Quarter symmetric finite element model of the uniaxial compression test. Specified boundary conditions were applied to entire surface being referred to

The shaded elements shown in Figure 16 identify the elements used for post-processing. The average X-strain and X-stress in the region were used to compare with the experimental data. RBCFAC had a major influence on the "re-stiffening" region of the stress-strain curve shown in Figure 17 while the value of $\overline{\varepsilon}_p^r$ influenced the stability of the model as the post peak softening region allowed for gradual redistribution of stress before element erosion rather than sudden deletion of the elements from the model. The best values of RBCFAC and $\overline{\varepsilon}_p^r$ were 1.25 and 0.0114 respectively. The result from the simulation using these values is shown in Figure 17.

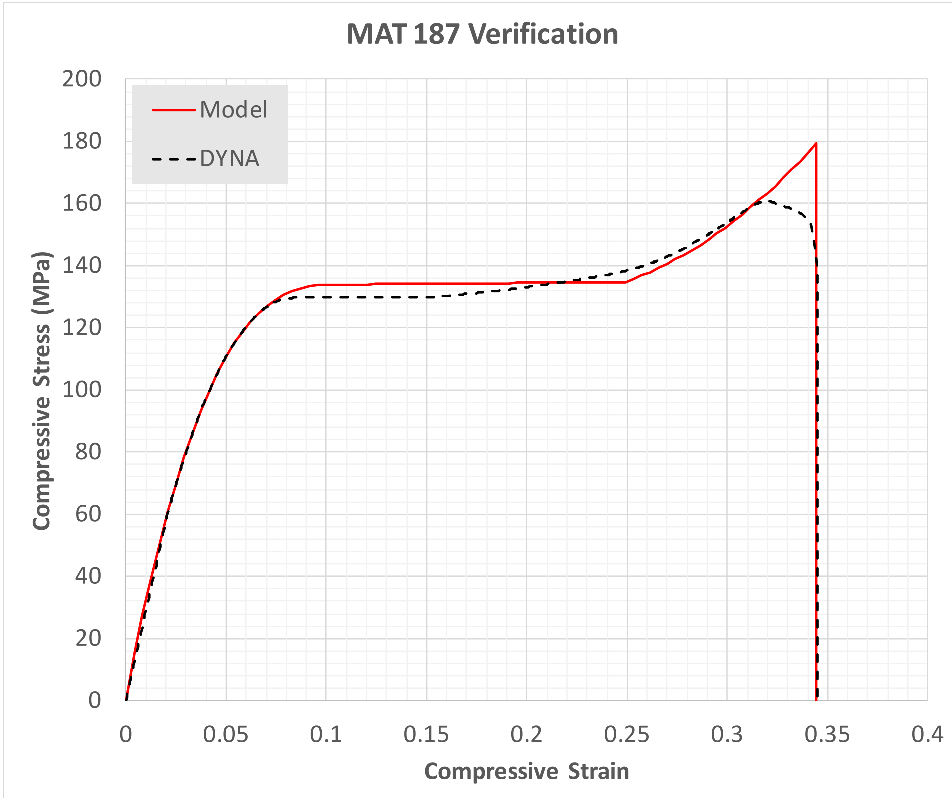

Figure 17. Result of multi-element compression simulation using RBCFAC=1.25 and $\bar{\varepsilon}_p^r$=0.0114.

Conclusions

The experimental techniques used to populate the *MAT_187 input deck for the F3900 epoxy resin were presented. Uniaxial tension, uniaxial compression, and uniaxial shear tests were performed and processed. Both single element and multi-element verification tests were performed to refine the input data that was challenging to obtain experimentally. Future work includes performing additional experiments on the F3900 composite resin, shear punch and torsion, to improve the available suite of data and provide more information to further refine the input deck. This research represents the first step of the overall goal of generate a tabulated failure surface through micromechanical virtual testing of the T800S/F3900 carbon fiber/epoxy resin unidirectional composite for use with *MAT_213. Additional experimental and modeling work will be performed to characterize the T800S carbon fiber and the carbon fiber/epoxy matrix interface.

Acknowledgements

Authors Shyamsunder, Khaled, and Rajan gratefully acknowledge the support of the Federal Aviation Administration through FAA Grant FAA grant 17-G-005 Amendment 002 titled “Enhancements to MAT_213 for Impact Analysis”, William Emmerling and Dan Cordasco, Technical Monitors. The authors would also like to thank Paul DuBois for the many helpful conversations.

References

D20 Committee. (2014). *Test Method for Tensile Properties of Plastics*. ASTM International.

D30 Committee. (2016). *Test Method for Compressive Properties of Polymer Matrix Composite Materials Using a Combined Loading Compression (CLC) Test Fixture*. ASTM International.

D30 Committee. (2019). *Test Method for Shear Properties of Composite Materials by the V-Notched Beam Method*. ASTM International.

Du Bois, P., Feucht, M., Haufe, A., and Kolling, S. (2006). "A generalized damage and failure formulation for SAMP." Keynote, Ulm, Germany.

Goldberg, R. K., Carney, K. S., DuBois, P., Hoffarth, C., Khaled, B., Shyamsunder, L., Rajan, S. D., and Blankenhorn, G. (2018). "Implementation of a tabulated failure model into a generalized composite material model." *Journal of Composite Materials*, 52(25), 3445–3460.

Hinton, M., and Kaddour, A. (2012). "The background to the Second World-Wide Failure Exercise." *Journal of Composite Materials*, 46(19–20), 2283–2294.

Hoffarth, C., Rajan, S. D., Goldberg, R. K., Revilock, D., Carney, K. S., DuBois, P., and Blankenhorn, G. (2016). "Implementation and validation of a three-dimensional plasticity-based deformation model for orthotropic composites." *Composites Part A: Applied Science and Manufacturing*, 91, 336–350.

Kaddour, A., Hinton, M., Smith, P., and Li, S. (2013). "The background to the third world-wide failure exercise." *Journal of Composite Materials*, 47(20–21), 2417–2426.

Khaled, B. (2019). "Experimental Characterization and Finite Element Modeling of Composites to Support a Generalized Orthotropic Elasto-Plastic Damage Material Model for Impact Analysis." Dissertation, Arizona State University, Tempe, AZ.

Khaled, B., Shyamsunder, L., Hoffarth, C., Rajan, S. D., Goldberg, R. K., Carney, K. S., DuBois, P., and Blankenhorn, G. (2018). "Experimental characterization of composites to support an orthotropic plasticity material model." *Journal of Composite Materials*, 52(14), 1847–1872.

Khaled, B., Shyamsunder, L., Hoffarth, C., Rajan, S. D., Goldberg, R. K., Carney, K. S., DuBois, P., and Blankenhorn, G. (2019). "Damage characterization of composites to support an orthotropic plasticity material model." *Journal of Composite Materials*, 53(7), 941–967.

Kolling, S., Haufe, A., and Feucht, M. (2005). "SAMP-1: A Semi-Analytical Model for the Simulation of Polymers." . *LS*, 27.

Liu, K., and Piggott, M. R. (1995). "Shear strength of polymers and fibre composites: 1. thermoplastic and thermoset polymers." *Composites*, 26(12), 829–840.

LS-DYNA keyword user's manual-Volume II: Material models. (2019). Livermore Software Technology Corporation, Livermore, CA.

Olsson, R. (2011). "A survey of test methods for multiaxial and out-of-plane strength of composite laminates." *Composites Science and Technology*, 71(6), 773–783.

Shyamsunder, L., Khaled, B., Rajan, S. D., Goldberg, R. K., Carney, K. S., DuBois, P., and Blankenhorn, G. (2020). "Implementing deformation, damage, and failure in an orthotropic plastic material model." *Journal of Composite Materials*, 54(4), 463–484.